
STRUCTURAL RESPONSE OF AMYLOID $A\beta_{11-42}$ DODECAMER FIBRIL TO MECHANICAL EXTENSION IN VACUUM

A PREPRINT

Ashkan Shekaari
 Department of Physics
 K. N. Toosi University of Technology
 Tehran, 15875-4416, Iran
 shekaari@email.kntu.ac.ir

Mahmoud Jafari *
 Department of Physics
 K. N. Toosi University of Technology
 Tehran, 15875-4416, Iran
 jafari@kntu.ac.ir

July 21, 2022

ABSTRACT

The mechanical strength of amyloid beta fibrils is correlated with neuronal cell death. Here, we resorted to steered molecular dynamics (SMD) simulations to mechanically deform the tertiary structure of the S-shaped amyloid beta $A\beta_{11-42}$ dodecamer fibril in vacuum, and then reported the resulting structural response of the fibril. A distribution of constant-velocity SMD trajectories was accordingly generated to stretch the fibril up to the points where it was ruptured. We started from the trajectory during which the maximum extension was achieved and therefore thoroughly investigated the associated structural changes, leading to the detection of the weakest amino-acid conjunctions at which the fibril is ruptured. The free energy needed for such a maximal extension was also estimated, showing that the initial fibrillar structure is indeed the energetically most-favorable conformation, in contrast to the maximally extended state, which was accordingly a rare event on the associated free energy profile. The structural properties were further investigated and discussed using constant-force SMD simulations, revealing stabilizing as well as destabilizing cores of the fibril in terms of the involved salt bridges. The applied replica-exchange umbrella sampling simulations finally measured the unfolding probability of the fibril, and accordingly uncovered the parallel rarity for the spontaneous unfolding of the system at the level of individual β -strands.

Keywords Alzheimer · Amyloid beta fibril · Mechanical strength · Steered molecular dynamics · Replica-exchange umbrella sampling

1 Introduction

Amyloid fibrils formed by misfolded protein aggregation have recently become a subject of extensive research due to their indubitable role in the pathogenesis of a number of neurodegenerative conditions [1] such as Alzheimer’s disease (AD) [2] and Parkinson’s disease (PD) [3]. These amyloid fibrils exhibit the structural feature in a way that they form one-dimensionally ordered structures [4], which are quite stable, and not easily dissolved in physiological conditions [5]. The structural stability of amyloid fibrils has been attributed to their β -sheet extended backbone conformation as a mechanically-resistant protein component [6].

The interesting mechanical properties [7, 8] of amyloid fibrils are indeed comparable to those of other mechanically-resistant, protein-based materials such as spider silk [9, 10]. Atomic force microscopy (AFM) experiments [11–14] have measured the elastic modulus of amyloid fibrils to be of the order of 1 GPa. Computational investigations have also estimated this property with values within 1–10 GPa [15–19]. The fracture toughness of amyloid fibrils with a length scale of 3 nm has also been calculated to be about 30 kcal/(mol.nm³) [20], which is comparable to that of the spider silk protein crystal with a length scale of 2 nm.

*Corresponding author

The mechanical properties of amyloid fibrils are indeed of immense value, particularly by taking into account the finding that they directly affect the biological function. As an illustration, the mechanical disruption of the cell membrane caused by amyloid fibrils [21] is due to the fact that its elastic modulus (~ 100 kPa [22]) is three orders of magnitude smaller than those of amyloid fibrils [23]. Investigating the mechanical properties of proteins and protein-based materials indeed provides a means to determine the pathways governing their unfolding/refolding processes when they are subject to mechanical traction. An optical tweezer-based force spectroscopy, for example, has been applied to investigate the mechanical unfolding and refolding of a single prion protein (PrP) in order to provide a deeper understanding of its misfolding mechanism, that directly contributes to the formation of amyloid oligomers as the nucleation seeds [24].

Based on the importance of mechanical properties of proteins and biomacromolecules, particularly the amyloid fibrils, the present work was therefore devoted to studying the biologically-important, yet-unmapped issue of structural and conformational responses of a single amyloid beta A β_{11-42} dodecamer fibril [25] (Fig. 1) to mechanical extension in vacuum via resorting to molecular dynamics (MD) simulations [26]. As the most recent form of amyloid fibrils, there are several key factors playing role in the stability of A β_{11-42} including the hydrogen bonding between the backbone amide groups of the two nearby chains, the van der Waals interaction between the top and the bottom β -sheets within the hydrophobic core, and the related salt bridges [27, 28]. Here, we exploited atomistic simulations to model the way a single A β_{11-42} dodecamer fibril responds structurally to external, deforming forces. The fibril was therefore stretched and undergone structural changes beginning from its initial, S-shaped, tertiary structure (Fig. 1) in a way that all the 12 chains were eventually aligned along the pulling direction as straightforward as possible to form the maximally-extended conformation in vacuum. Sec. 2 describes the applied computational setup in more detail.

2 Computational details

Steered molecular dynamics (SMD) [29] simulations were applied to investigate the response mechanism of an amyloid beta dodecamer fibril (A β_{11-42}) to mechanical extension in vacuum using both constant velocity (cv) and constant force (cf) protocols. The initial atomic positions of A β_{11-42} were taken from the RCSB [30] Protein Data Bank (PDB) with the entry code 2MXU [31]. All the simulations were carried out, in parallel, using NAMD (version 2.14b2) [32] with the July 2018 update of the CHARMM36 force fields [33], on Debian-style [34] Linux [35] systems supported by MPICH (version 2-1.4) [36, 37]. The fibril was solvated in a water box under periodic boundary conditions with a unit-cell padding of 2.0 nm to decouple the periodic interactions. The minimization simulation was then carried out for 50000 conjugate gradient steps (100 ps) followed by a 2-ns, free-dynamics equilibration at 310 K and 1.01325 bar. Langevin forces with a Langevin damping constant of 2.50/ps along with the Langevin piston pressure control were applied for the NPT equilibration to keep the temperature and pressure of the system fixed during the simulations.

After equilibration, the next SMD simulations were carried out, in vacuum, with both the thermostat and the barostat turned off in order to not to disturb the atomic movements. For cv simulations, the C $_{\alpha}$ atom of the N-terminus tail [located on the first chain (A), first residue (11), the amino acid Glu, all abbreviated as Glu $_{A}^{11}$:C $_{\alpha}$] of the fibril is kept fixed, while that from the C-terminus tail (Ala $_{L}^{42}$:C $_{\alpha}$) is pulled along $+z$, perpendicular to the fibril axis, as illustrated in Fig. 1. A pulling velocity (v_p) distribution containing values ranging from 10^{-2} to 10 Å/ps were tested to reach the optimized, slow-enough value (0.1 Å/ps) for which the maximum elongation (Fig. 2) was achieved and therefore the pulling process was reversible in a way that the associated pulling work was equivalent to the free energy difference (ΔG) between the initial and final states. For the cv simulations, different values including 0.8, and 1 to 10 kcal/(mol.Å 2) were assigned to the spring constant (k_s) with an increment of about 0.5 kcal/(mol.Å 2)—corresponding to a thermal fluctuation of $\sqrt{k_B T/k_s} = 1.11$ Å for the SMD atom at 310 K; k_B being the Boltzmann’s constant—which accordingly led to the total number of 20 cv simulations with the accumulative time of 75.5 ns. The integration time step was 1 fs. The hydrogen bonds were identified within the hydrogen donor-acceptor distance of 3 Å and the cutoff angle of 20°. The O–N distance cutoff for salt-bridge identification was also set to 3.2 Å. The solvent-accessible surface area (SASA, nm 2) [40] was calculated using the rolling-ball algorithm [41], with a radius of 1.4 Å for the probe sphere. The force acting on the SMD atom was described by

$$\mathbf{f}(\mathbf{r}, t) = -\nabla U(\mathbf{r}, t) = -\nabla \left(\frac{k_s}{2} [v_p t - (\mathbf{r} - \mathbf{r}_0) \cdot \mathbf{n}]^2 \right),$$

where U is the harmonic potential (spring), t is time, \mathbf{r} and \mathbf{r}_0 are respectively the instantaneous and initial position vectors of the SMD atom, and $\mathbf{n} = (0, 0, 1)$ is the normalized pulling vector along $+z$ (bold characters denote vectors). The VMD program was also used to post-process and analyze the outputs. We used the Jarzynski’s equality [42]:

$$e^{-\beta \Delta G} = \langle e^{-\beta W} \rangle, \quad (1)$$

to approximate the equilibrium free energy difference (ΔG) between the initial (folded) and final (extended) conformations, where $\beta = 1/k_B T$ is inverse temperature of the surrounding. The work (W) distribution, done through

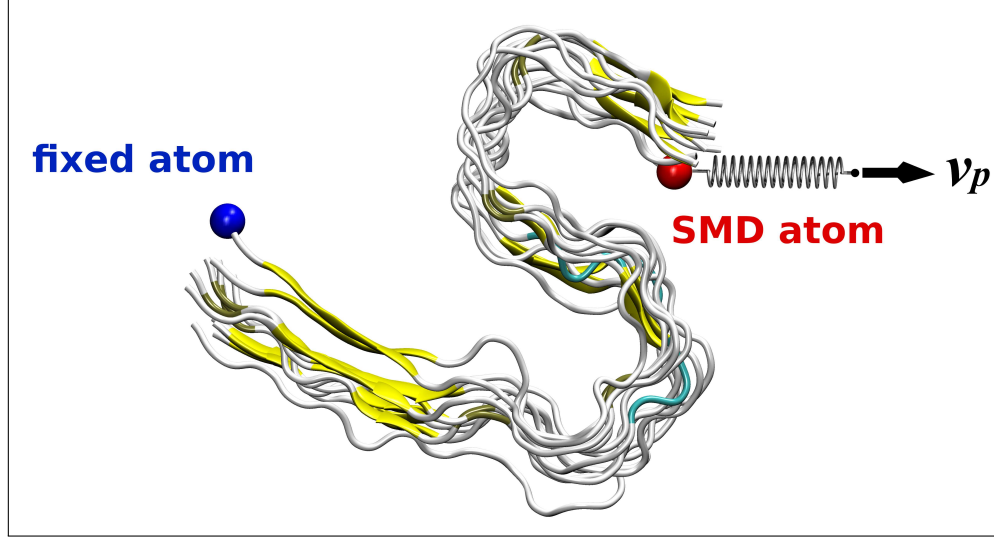


Figure 1: The tertiary structure of S-shaped amyloid beta (A β_{11-42}) dodecamer fibril—rendered in VMD [38] using Tachyon parallel/multi-processor ray tracing system [39]. The fixed and SMD atoms at the two ends of the fibril are shown by the blue and red balls, respectively. The moving guiding potential applied in the pulling experiments is also represented by a spring connected to the C-terminus and is pulled with the constant velocity of v_p .

non-equilibrium processes, stretched the fibril up to the points where it collapsed, and were calculated via numerical integration of the corresponding, time-dependent forces exerted on the SMD atom simply by $W \simeq v_p \Delta t \sum_i f(t_i)$, where the integration time was $\Delta t = 10$ fs. For cf-SMD simulations, three values including 500, 1000, and 2000 pN were used and applied along $+z$ (\hat{n}), each for 5 ns, during which the end-to-end extension (EEE) of the fibril was mapped.

Replica-exchange umbrella sampling (REUS) [43] simulations were also applied to estimate the potential of mean force (PMF) associated to one-dimensional stretching of a single β -strand of the fibril. The end-to-end extension of the strand, namely the distance between Glu¹¹:C α and Ala⁴²:C α , was defined as the reaction coordinate (collective variable), which increased from 31.40 to about 42.40 Å using SMD according to the function $31.4 + i$, where i is an integer and runs from 0 to 11, leading to 12 replicas as well. We accordingly used the weighted histogram analysis method [44] implemented in WHAM (version 2.0.10.2) [45] to recover the unbiased PMF. The harmonic biasing potential of the form $U(\xi, i) = k(\xi - \xi_i)^2/2$ was applied, where $k = 2$ kcal/(mol.Å²), ξ is the reaction coordinate, and $\xi_i = (31.4 + i)$ Å defines the center of the i th bias potential. The time-step was set to 1 fs, and each replica was independently equilibrated for 1 ns at 310 K in a way that the associated time-dependent total energy curves of all the replicas exhibited converging patterns with long tails over the last 0.5 ns of the trajectories [46]. The WHAM code was instructed to divide the reaction coordinate (ξ) into 17 bins for analysis, each with the window length of 1 Å, starting from 28.5 and ending at 45.50 Å, with the convergence threshold of 10^{-6} .

3 Results and discussion

3.1 cv-SMD simulations

3.1.1 The maximum-extension trajectory

During equilibration, the fibril remained stable with a C α root-mean-square deviation (RMSD) of less than 6.5 Å and with the all-atom RMSD of < 7 Å from the reference crystal structure. For cv simulations, the dummy atom, attached to the SMD one via the spring with the constant of k_s , is pulled at the constant velocity of $v_p = 0.1$ Å/ps along $+z$, which accordingly makes the SMD atom to experience a force linearly dependent on the distance between the both atoms. In this section (Sec. 3.1.1), we exclusively discuss the results obtained for the simulation with $k_s = 2$ kcal/(mol.Å²), for which the maximum extension of 53.387 nm was achieved. Fig. 2 shows the trajectory of the SMD atom in both $x - z$ and $y - z$ Cartesian planes during the simulation.

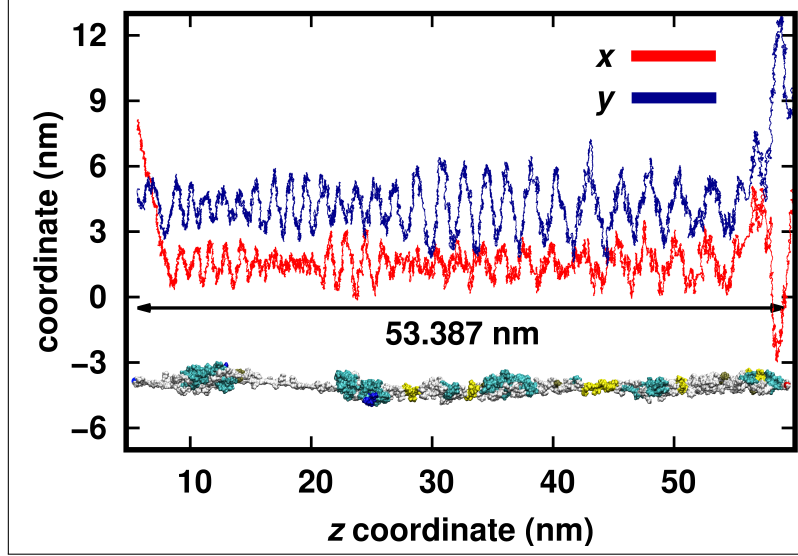


Figure 2: The trace of the SMD atom in the $x - z$ (red) and $y - z$ (blue) Cartesian planes during the simulation—generated by Gnuplot (version 5.2) [47]. The fluctuating pattern in the $x - y$ plane is clearly related to the S-shape structure of the fibril. This maximum elongation (53.387 nm) was achieved for $k_s = 2.0 \text{ kcal}/(\text{mol} \cdot \text{\AA}^2)$ and $v_p = 0.1 \text{ \AA}/\text{ps}$.

The fluctuating pattern is obviously a consequence of the S-shape structure of the fibril in the $x - y$ plane, making the SMD atom to move on a chiral path in three dimensions. The ever-decreasing part of the $z - x$ diagram from the beginning to the point where the fluctuations begin corresponds to the alignment of the end-to-end axis (connecting the fixed and SMD atoms) along the pulling direction ($+z$). During the simulation, the SMD atom travels a net distance of about 46.177 nm ($= 53.387 \text{ nm} - 7.21 \text{ nm}$, where the latter is the initial distance between the fixed and SMD atoms at $t = 0$), leading to the maximum elongation, as visualized in Fig. 2.

Fig. 3 provides more details about changes in the secondary structure of the fibril.

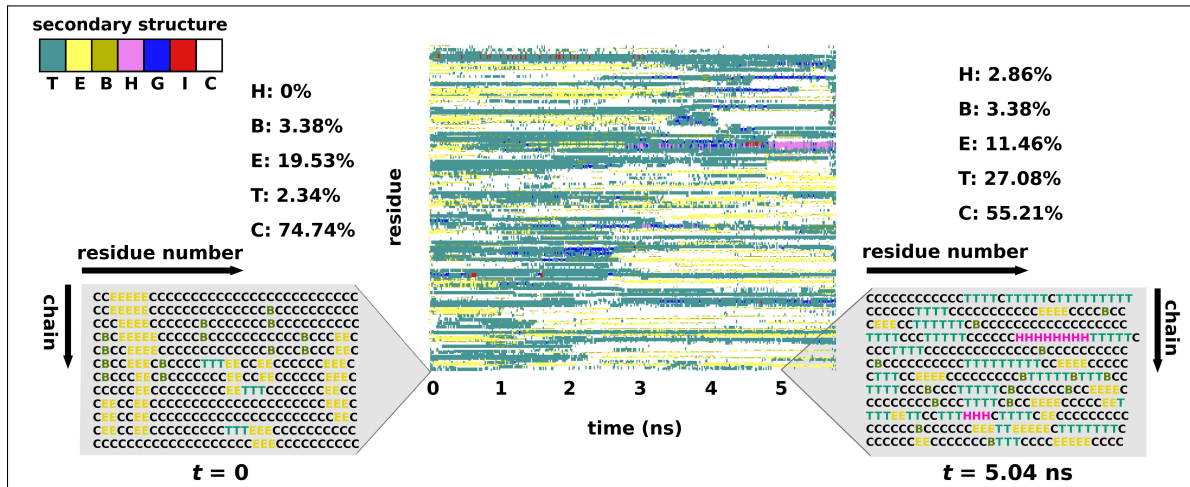


Figure 3: Evolution in the secondary structure of the fibril during the simulation—rendered in VMD using the Timeline plugin and edited by GIMP 2.8 [48]. The character-based representations correspond to the secondary structure at $t = 0$ (the equilibrated fibril in solution) and at $t = 5.04 \text{ ns}$ at which maximum elongation (53.387 nm) has been achieved. The residue axis starts from Glu_A¹¹ at the top and ends to Ala_L⁴² at the bottom. E, B, H, G, I, and C, used by STRIDE algorithm [49] respectively stand for the Turn, Extended, isolated Bridge, α -Helix, 3_{10} -helix, π -helix, and Coil, and their contributions to the total secondary structure have also been shown by the percent values. The rows and columns in the character-based representations respectively show the chains (A to L) and residue numbers (11 to 42).

As is seen, most of the diagram is filled by the green and white areas, which respectively correspond to Turn and Coil. Examining the two character-based representations further reveals that during the extension, the Coil content decreases by 19.53%, while that of the Turn rises by 24.74%. The Extended content also reduces by 8.07%, while that of the α -Helix increases from zero to 2.86%. Comparing the $t = 0$ representation (corresponding to the pre-equilibrated fibril in solution) and that of the crystal structure demonstrates that equilibration in water dramatically decreases the Extended content from 62.5% to 19.5%.

Examining the per-residue root-mean-square fluctuation (RMSF) and RMSD of the fibril during the simulation could also be interesting, as shown in Fig. 4. The most varying (flexible) residues are those starting from Hsd $_{\text{D}}^{14}$ (Hsd for

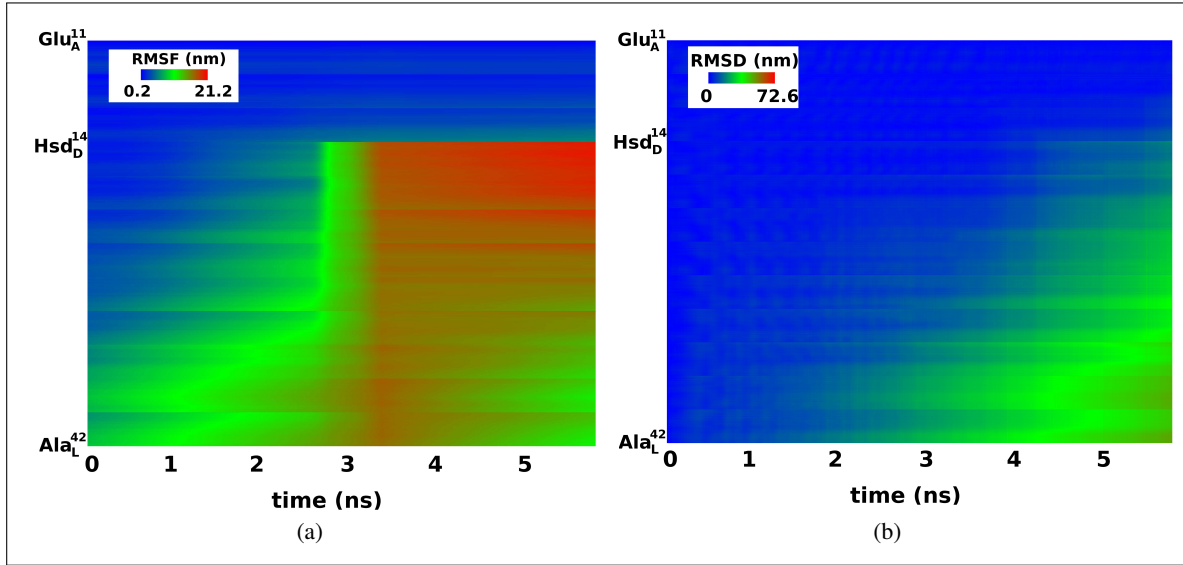


Figure 4: The per-residue (a) RMSF, and (b) RMSD of the fibril during the simulation. Variations begin from Hsd $_{\text{D}}^{14}$ and 2.5 ns on. The fibril also collapses at 5.04 ns corresponding to the maximum elongation.

histidine, 14 for the residue number, and D for the chain name) to the last one (Ala $_{\text{L}}^{42}$), as covered by the red region of Fig. 4(a). The blue region, from Glu $_{\text{A}}^{11}$ to Hsd $_{\text{D}}^{14}$, indicates the least-flexible residues during the extension, based on the fact that they are the farthest amino acids from the SMD atom. Fig. 4(b) shows these residues within the same range as inferred from Fig. 4(a), with nearly vanishing RMSD values. The RMSDs of the rest of the residues do not change over the first 2 ns, however, from then on, they take an increasing trend in a way that the more a residue is closer to the SMD atom, the larger its RMSD.

Fig. 5(a) illustrates the total RMSD of the fibril as a function of time.

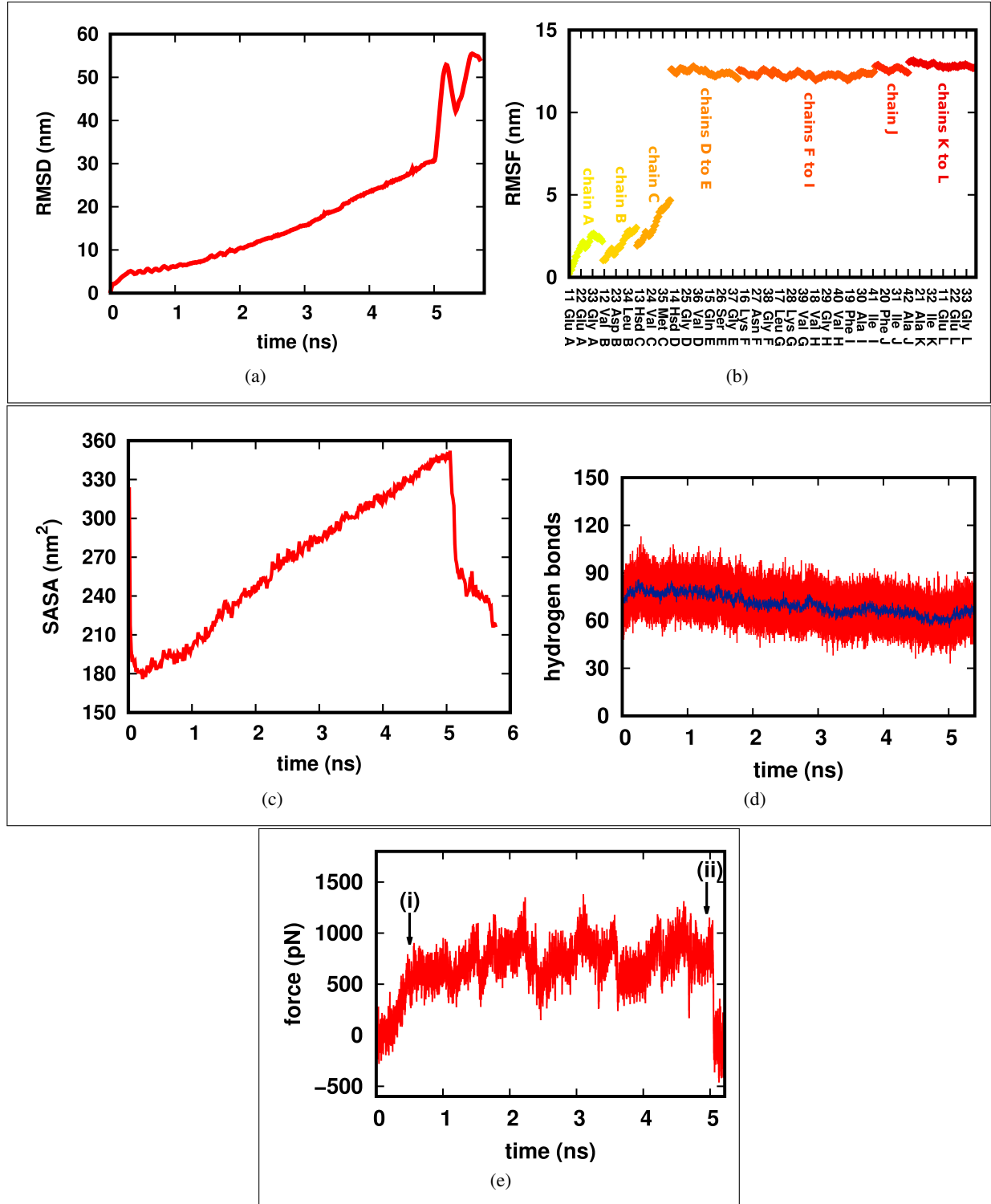


Figure 5: (a) Total RMSD, (b) per-residue RMSF, (c) SASA, (d) number of hydrogen bonds, and (e) the force exerted on the SMD atom, during the simulation. The instances labeled by the arrows (i) and (ii) denote the points at which the fibril begins to extend and approaches its maximum length, respectively.

As is seen, the total RMSD takes an increasing trend up to 5.04 ns (corresponding to the maximum extension) with a value of about 31 nm at this point, in agreement with the RMSD value of the green area in Fig. 4(b). From then

on, however, an irregular, fluctuating pattern takes place due to the rupture of the fibril. Fig. 5(b) exactly shows the mostly-unchanged as well as the mostly-flexible residue ranges consistent with what was seen in Fig. 4(a). The RMSF exhibits a drastic, stepwise increase of about 8 nm at the place of Hsd $_{D}^{14}$ (more exactly, at the interface of Ala $_{C}^{42}$ and Glu $_{D}^{11}$), which unmistakably reveals the weakest point at which the fibril is ruptured. The parts with different colors further illustrate that the stepwise pattern, for other possible (k_s or v_p) distributions, would take place at the joining points of the chains. The chains K and L exhibit the largest RMSF values due to being nearest to the SMD atom according to the fact that the more a residue is closer to the SMD atom, the larger its RMSF.

Fig. 5(c) shows the time dependence of SASA associated to the fibril during the simulation. It is seen that the time interval from $t = 0$ up to the global minimum (at about 0.2 ns) corresponds to the alignment of the end-to-end axis along $+z$. The why of this minimum in SASA is as such related to the fact that the fibril, over this interval, is being relaxed and equilibrated in vacuum starting from the initial, pre-equilibrated conformation in solution. Indeed, during equilibration in solution, water molecules have randomly been distributed around the fibril and more importantly within the intrastrand regions (i.e., between the chains), which increase the space between any two consecutive chains, leading to a value of about 320 nm 2 at $t = 0$ as well. For $t > 0$, in contrast, the solution was removed, and up to 0.2 ns, during which the extension has not yet started, the fibril is equilibrated in vacuum and the intrastrand spaces accordingly become smaller. As a direct consequence, SASA takes a decreasing trend from $t = 0$ on, and is globally minimized at about 0.2 ns. The global maximum in the moving average of the number of hydrogen bonds [Fig. 5(d)] occurs exactly based on the same reasoning: removing water molecules from the intrastrand spaces makes the chains to get closer to each other and consequently increases the number of hydrogen bonds within these regions, leading to the maximum number of hydrogen bonds at the minimum of SASA. Indeed, variations of the SASA and the number of hydrogen bonds are intrinsically consistent with each other. Extension up to 53.387 nm corresponds to increase/decrease in the SASA/number of hydrogen bonds, with a nearly-linear time dependence. The maximum of SASA also reveals the instance at which the fibril approaches its maximum length corresponding to the minimum in the number of hydrogen bonds after which the fibril is being ruptured.

The time dependence of the force exerted on the SMD atom has finally been shown in Fig. 5(e) during the simulation, demonstrating that, due to the pulling, the fibril begins to rotate from $t = 0$ on, until the end-to-end axis is entirely directed along the pulling direction ($+z$) at the instance denoted by the arrow (i). From then on, the extension fully starts, during which the acting bonds (the hydrogen and the van der Waals bonds, and the salt bridges) within the fibril are ruptured and reformed constantly, leading to the saw-tooth pattern from (i) to (ii) as well. The instance labeled by the arrow (ii) also corresponds to the maximum elongation after which the fibril is accordingly ruptured and the force then immediately vanishes.

3.1.2 Free energy estimation

Table 1 illustrates the calculated work (W) values for the present k_s distribution, needed to maximally stretch the fibril. Larger values of W obviously correspond to larger extensions according to $W \simeq v_p \Delta t \sum_i f(t_i) = (X(t) - X_{eq}) \sum_i f(t_i)$, where $X(t) = X_{eq} + v_p \Delta t$ is the distance between the fixed and SMD atoms, and $X_{eq} = 7.21$ nm at $t = 0$ [the net elongation is therefore $X(t) - X_{eq}$]. Table 1 contains the time (t_r) and length (X_r) values associated to the rupture of the fibril for the present k_s distribution.

As expected, the maximum work value belongs to $k_s = 2$ kcal/(mol. \AA^2), namely the maximum extension. Examining the last column could be interesting according to which: (i) the weakest amino-acid conjunctions are the Ala 42 -Glu 11 pairs over the different chains; (ii) the weakest Ala 42 -Glu 11 pair is that between the chains I-J respectively based on the fact that it contributes 30% to the rupture of the fibril; and (iii) the other contributions are respectively 15% for J-K and E-F, 10% for A-B and B-C and G-H, and 5% for C-D and F-G.

Applying the Jarzynski's equality (Eq. 1) to the calculated W distribution provided an estimation of about $\Delta G = 679.828 k_B T$ at 310 K as the free energy needed to maximally stretch the fibril. Within solution, even larger free energy is needed for such an extension based on the observation that enhancement in entropy of the solvent (water) molecules expelled from the hydrophobic core between the two β -sheets (i.e., the hydrophobic effect) is key to the fibril's stability [50]. To put this value into perspective, it is equivalent to the hydrolysis of about 151 adenosine triphosphate (ATP) molecules. In terms of force, the average force to stretch the fibril using values of Fig. 5(e) is about 750 pN, while the one needed to unzip a double-stranded DNA is only ~ 12 pN [51]. Such a large value unmistakably reveals that this kind of unfolding could not then happen spontaneously (e.g., triggered by thermal fluctuations within the physiological conditions) due to having a much small probability of about $\exp(-\beta \Delta G) = \exp(-679.828) \sim 5.68 \times 10^{-296}$.

Based on the observation that each of the separated parts refolded after the ruptures, we also accordingly modeled the fibril as a spring obeying the Hooke's law in a way that the associated potential energy is given by $\Delta U = k_f (X - X_{eq})^2 / 2$, where k_f is the spring constant of the fibril itself, and $X - X_{eq}$ is the maximum traction length.

Table 1: The calculated times (t_r) and lengths (X_r) for the k_s distribution at which the fibril was ruptured. The associated W distribution needed for such maximal extensions is also tabulated in the fourth column. Approximating the fibril as a spring obeying the Hooke's law according to the W distribution resulted in the k_f values as the constants of the fibril's analogue springs. The last column also contains the conjunction points at which the ruptures take place.

k_s (kcal/mol.Å ²)	t_r (ns)	X_r (nm)	W ($k_B T_{310}$)	k_f (kcal/mol.Å ²)	conjunction
0.8	1.30	15.81	1065.129	0.468	Ala _J ⁴² -Glu _K ¹¹
1.0	3.11	34.00	2832.817	0.128	Ala _F ⁴² -Glu _G ¹¹
1.5	1.20	15.78	721.946	0.319	Ala _I ⁴² -Glu _J ¹¹
2.0	5.04	53.38	8014.233	0.122	Ala _C ⁴² -Glu _D ¹¹
2.5	2.12	24.71	1706.532	0.181	Ala _E ⁴² -Glu _F ¹¹
3.0	2.18	25.41	2110.711	0.207	Ala _I ⁴² -Glu _J ¹¹
3.5	2.44	27.90	2066.677	0.157	Ala _I ⁴² -Glu _J ¹¹
4.0	2.27	26.40	2650.802	0.234	Ala _A ⁴² -Glu _B ¹¹
4.5	1.77	21.44	1725.039	0.276	Ala _J ⁴² -Glu _K ¹¹
5.0	1.11	14.91	795.878	0.436	Ala _B ⁴² -Glu _C ¹¹
5.5	3.84	42.06	3944.942	0.106	Ala _E ⁴² -Glu _F ¹¹
6.0	4.39	47.24	5310.415	0.108	Ala _I ⁴² -Glu _J ¹¹
6.5	1.79	21.65	1999.447	0.311	Ala _B ⁴² -Glu _C ¹¹
7.0	1.70	20.87	1519.529	0.264	Ala _I ⁴² -Glu _J ¹¹
7.5	1.82	21.89	1759.888	0.265	Ala _A ⁴² -Glu _B ¹¹
8.0	2.30	26.68	3025.168	0.259	Ala _C ⁴² -Glu _H ¹¹
8.5	3.76	41.23	4693.728	0.132	Ala _E ⁴² -Glu _F ¹¹
9.0	0.75	11.37	676.834	1.271	Ala _I ⁴² -Glu _J ¹¹
9.5	1.46	18.23	1385.817	0.370	Ala _G ⁴² -Glu _H ¹¹
10.0	2.73	30.61	2993.430	0.178	Ala _J ⁴² -Glu _K ¹¹

Replacing ΔU with the W values of Table 1, and using the associated X_r values, the related k_f distribution was then determined, showing that A β_{11-42} behaves, on average, like a spring. Remembering the equivalence between W and the corresponding ΔG due to slow-enough, then reversible pullings, the average value of k_f was also estimated as follows for the present distribution of the trajectories:

$$\langle k_f \rangle = \sum_{i=1}^{20} k_{f_i} e^{-\beta W_i} / \sum_{i=1}^{20} e^{-\beta W_i} = 1.270 \text{ kcal/mol.Å}^2.$$

Examining the time dependence of the van der Waals energy (E_{vdW}) for the present k_s distribution could also be interesting, as shown in Fig. 6.

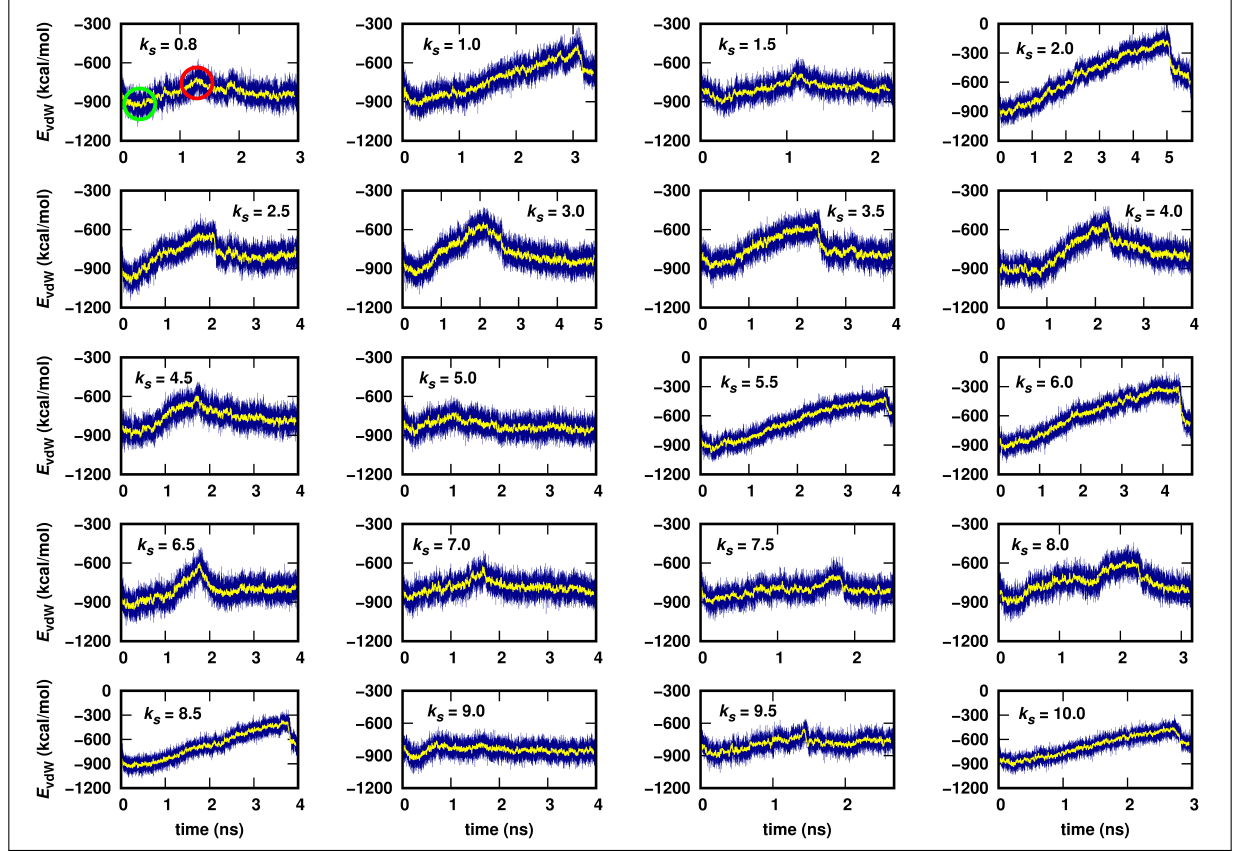


Figure 6: The time dependence of E_{vdW} during the cv-SMD simulations. The k_s changes from 0.80 to 10 kcal/(mol.Å²), and the moving averages are shown by yellow curves. The maximums of the diagrams correspond to the associated maximum extensions depending on k_s . The minimum and maximum points are also typically marked by the green and red circles in the top-left diagram ($k_s = 0.8$), respectively. All the minimums evidently take place at about 0.2 ns

A unique, three-stage pattern is seen in all the diagrams: (i) decrease from $t = 0$ to the global minimum at about 0.2 ns; (ii) increase from the minimum to the maximum point during which the fibril approaches its maximum length; and (iii) decrease from the maximum point on. The first decreasing trend obviously takes place based exactly on the reasoning provided for explaining the time dependence of SASA [Fig. 5(c)] over the same time interval. At the minimum points, the fibril is in its most stable conformation due to being equilibrated in vacuum.

During the second stage, however, the fibril becomes increasingly unstable with time. Evidently, the maximum point corresponds to the maximum extension, and therefore, to the least stability. After the fibril is ruptured at this point, each separated part begins to refold, and E_{vdW} consequently seeks a second minimum. By taking into account the fact that X linearly depends on time [$X(t) = X_{eq} + v_p t$], the same brands of behavior could then be inferred for E_{vdW} as a function of X . As a result, the minimums of $E_{vdW}(t)$ indicate equilibrium states, and the variation of E_{vdW} around them could then be approximated by that of a simple harmonic oscillator, revealing the spring-like feature (reversibility) of the fibril under mechanical traction. In terms of statistical mechanics [52], the more the fibril is stretched, the less the number of accessible conformations [i.e., microstates (Ω)]. The associated conformational entropy (S) of the fibril according to the Boltzmann's formula ($S = k_B \ln \Omega$) then becomes minimum/maximum at the maximum/minimum of $E_{vdW}(t)$.

3.2 cf-SMD simulations

The three constant forces including 500, 1000, and 2000 pN were applied along $\hat{n} = (0, 0, 1)$ using the same fixed and SMD atoms. The total time-span for each of the three cf-SMD trajectories is 5 ns. Fig. 7(a) illustrates the time dependence of EEE (the end-to-end extension of the fibril) during the simulations.

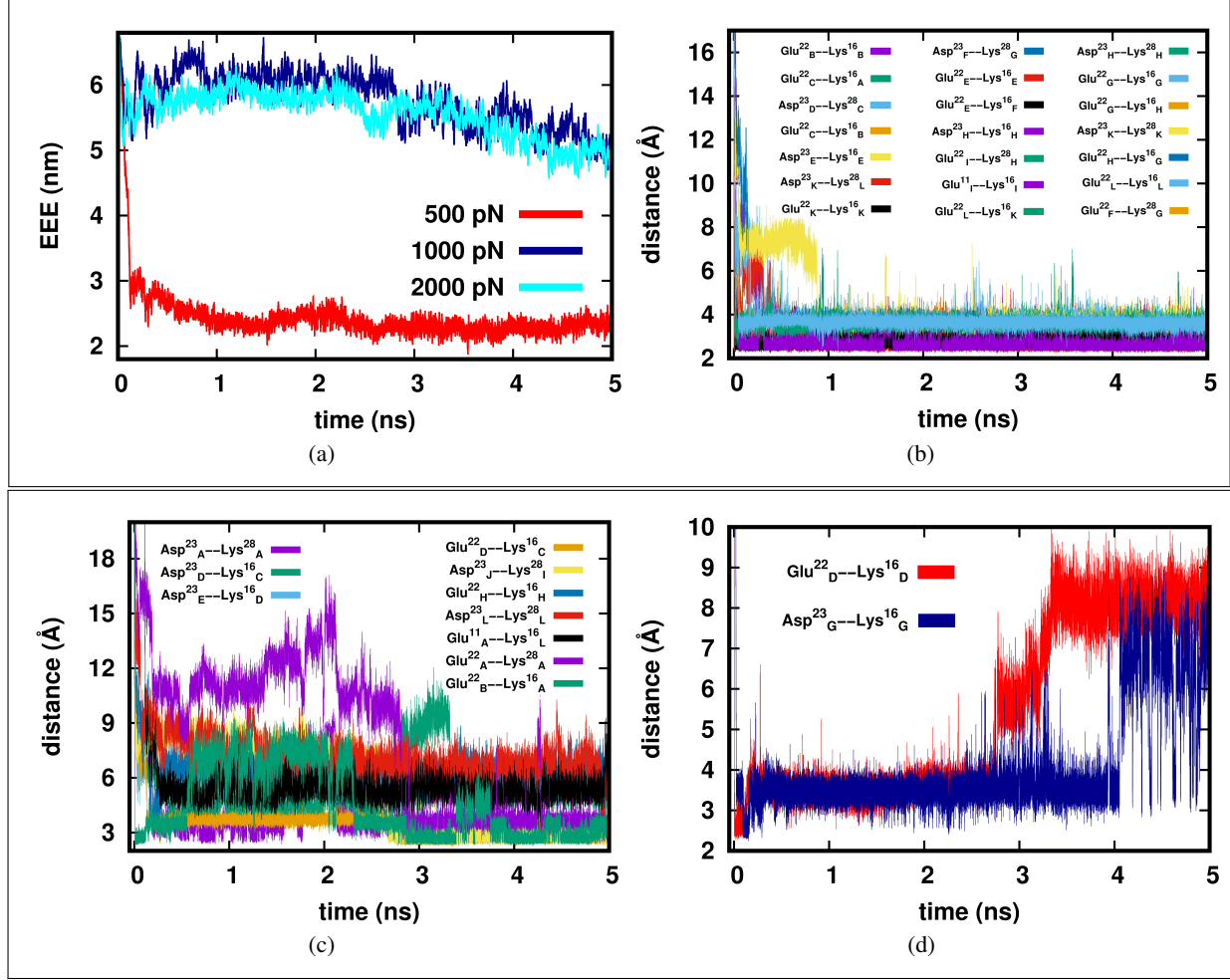


Figure 7: The time dependence of (a) EEE_f for constant forces of 500 (red), 1000 (blue), and 2000 pN (cyan) during the three cf-SMD simulations, and (b, c, d) salt bridges for the 500-pN simulation. These thirty three salt bridges fall into three categories in a way that (b) includes twenty one bonds with marked converging patterns over the last 4 ns within 2–4 Å; (c) with ten bonds which fluctuate largely between 2 and 18 Å; and (d) with only two interstrand salt bridges with dramatic variations over the last 2.5 ns.

For 500 pN, a clear, exponentially-decaying pattern is observed with a relatively long, converging tail over the last 2.5 ns. Examining the time dependence of the associated salt bridges could also be illustrative. We classified the obtained thirty three salt bridges into three groups depending on their time dependence behaviors. The first one [Fig. 7(b)] includes twenty one salt bridges with very exact converging patterns over the last 4 ns of the trajectory within the narrow range of 2–4 Å, and therefore have the leading contributions to the structural stability of the fibril, as well as to the smooth converging tail of the related EEE. These pairs indeed function as a "lock" to maintain the fibril's integrity.

The second group, shown in Fig. 7(c), includes ten bonds, which some of them fluctuate largely over the total time-span, some evolve dramatically over the first 2.5 ns and then converge, and the rest exhibit converging trends to values > 5 Å nearly over the entire trajectory. The associated collective effect of such bonds manifests itself in the form of a gentle fluctuation in the related EEE over the first 2.5 ns.

The last group [Fig. 7(d)] includes only two interstrand salt bridges, which show converging patterns over the first 2.5 ns within 3–4 Å, however, with anomalous fluctuations between 3 and 10 Å from then on. They could accordingly be considered as the core of the structural instability of A β_{11-42} , revealed at the scale of 500 pN.

Applying a stronger force of 1000 pN, however, led to a radically-different pattern for EEE [Fig. 7(a)], and both inter and intrastrand salt bridges underwent dramatic changes compared to 500 pN. Likewise, they also fall into three categories, as seen in Fig. 8.

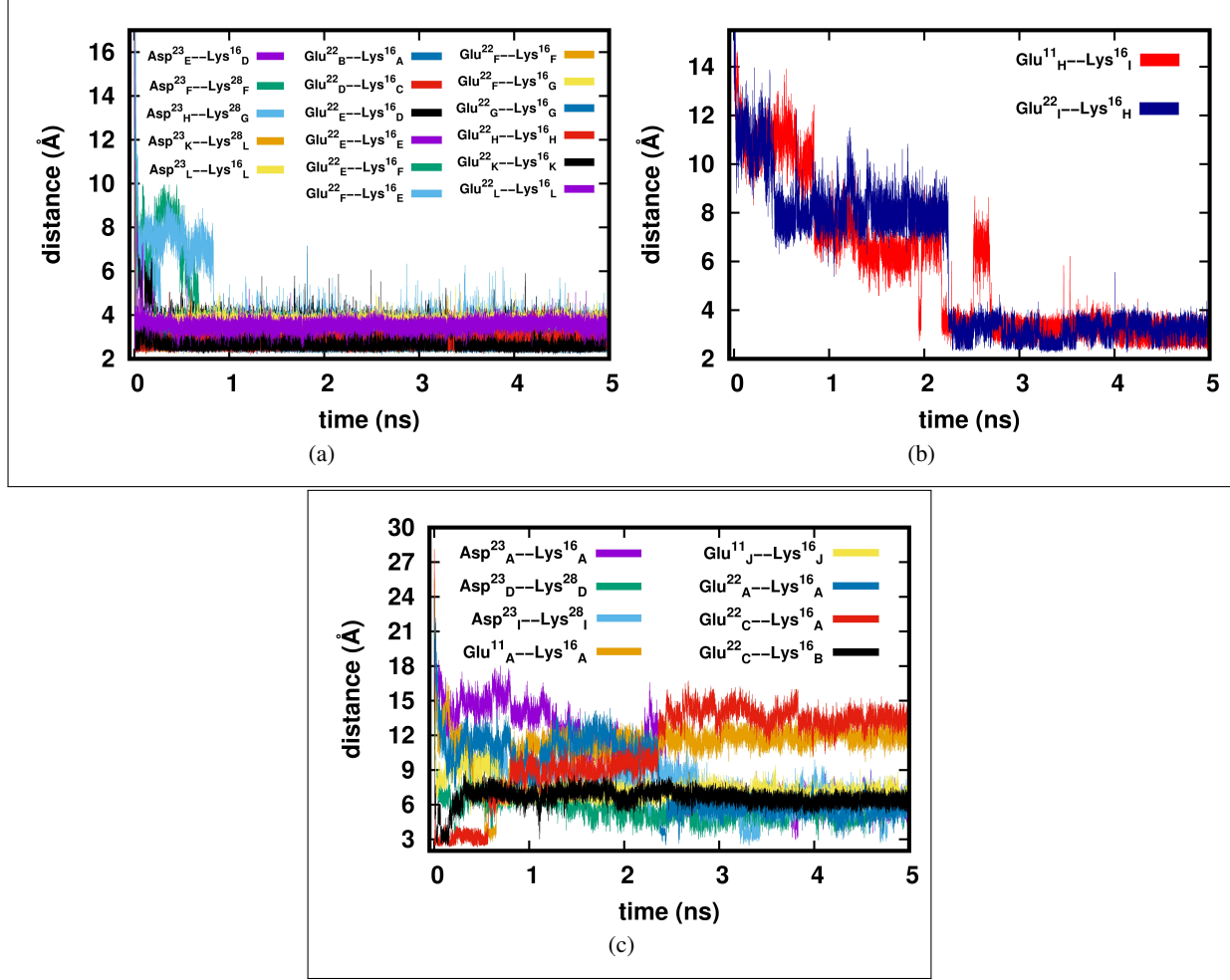


Figure 8: The time dependence of the salt bridges identified at the scale of 1000 pN during the second cf-SMD simulation. (a) includes seventeen bonds with very clear converging patterns over the last 4 ns within the narrow interval of 2–4 Å. (b) includes only two bonds between the chains H and I with large variations over the first 2.5 ns. (c) includes eight salt bridges with anomalously large fluctuations within 2–18 Å over the entire time-span and mostly contribute to the instability of the fibril.

The first group [Fig. 8(a)], including seventeen bonds out of twenty seven, are those uniformly fluctuate within 2–4 Å over the last 4 ns of the trajectory, and therefore, contribute the most to the structural stability. The second category [Fig. 8(b)], composed of only two intrastrand bonds between the chains H and I, shows converging patterns over the last 2.5 ns within 2–4 Å with a marginal impact on the fibril’s stability due to being less in number as well as being formed between only two chains. The last group, illustrated in [Fig. 8(c)], includes eight salt bridges, which some of them fluctuate unstably over the total time-span, and the rest converge to values > 6 Å. These bonds indeed significantly contribute to the overall structural instability of A β_{11-42} at the level of 1000 pN of the pulling force. Compared to 500 pN, the latter (1000 pN) reduces the number of stable bonds in the first and second categories by 19% and 80%, respectively, while increases that of the third group (destabilizing bonds) by 4 times, leading to a remarkable rise of about 3.38 nm in the EEE from 2.33 nm (at 500 pN) to 5.71 nm (at 1000 pN) on average. All the salt bridges were formed between Asp²³, Glu²², Lys¹⁶, and Lys²⁸, which are among the most commonly-observed bonds with leading contributions to the stability of entropically unfavorable folded conformations of the fibril.

From 1000 to 2000 pN, nevertheless, no overall change is interestingly observed [Fig. 7(a)], demonstrating that at this force level, there exists very similar classes of salt bridges, which leave the EEE pattern of 1000 pN nearly intact.

3.3 REUS simulation of a single β -strand

Table 2 contains the free energy difference (ΔG) of an individual β -strand as a function of the reaction coordinate (ξ) defined as the distance between the first (Glu¹¹:C $_{\alpha}$) and the last (Ala⁴²:C $_{\alpha}$) atom (more details have been provided in Sec. 2). We aim at mapping the associated free energy difference to inquire into the unfolding probability of the fibril at the single-strand level.

Table 2: Variation in the free energy (ΔG) of the system as a function of the reaction coordinate (ξ) defined as the distance between the first and the last atoms of the β -strand. The maximum free energy difference takes place at 37 Å.

ξ (Å)	ΔG (kcal/mol)
29	3.199933
30	7.474884
31	11.108003
32	14.171684
33	16.583810
34	18.437609
35	19.743706
36	20.409997
37	20.480211
38	20.010008
39	18.943731
40	17.237645
41	14.983855
42	12.171738
43	8.708064
44	4.674948
45	0.000000

According to the table, the maximum free energy difference takes place at 37 Å, for which $\Delta G_{max} = 20.48$ kcal/mol = $12.61 k_B T$ at 310 K, corresponding to the net extension of 5.1 Å ($= 36.5 - 31.4$, where the latter is the initial C $_{\alpha}$ -C $_{\alpha}$ distance). Plugging this ΔG_{max} into the Boltzmann’s factor results in $\exp(-12.61) \sim 3.34 \times 10^{-6}$, indicating that the extension of a single β -strand of A β_{11-42} fibril by such a small value of 5.10 Å is also a rare event, albeit needing an energy equivalent to the hydrolysis of only about three ATP molecules for an external agent in vacuum.

4 Conclusions

Steered molecular dynamics (SMD) simulations were applied to deform the tertiary structure of A β_{11-42} fibril in the form of extensions in vacuum in order to inquire into the resulting structural response. Constant-velocity SMD simulations, with the pulling velocity of 0.1 Å/ps, and with the spring constant distribution within 0.8–10 kcal/(mol.Å²), were accordingly carried out to stretch the fibril up to the points where it was ruptured. Within the present distribution, the trajectory that led to the maximum extension (namely, 53.387 nm) was broadly investigated via analyzing a number of important MD indicators including RMSF, RMSD, secondary structure, SASA, number of hydrogen bonds, and the force exerted on the SMD atom, during the simulation. As a result, the weakest amino-acid conjunctions, namely the Ala⁴²-Glu¹¹ pairs formed between different, consecutive chains, were detected at which the fibril was ruptured. The free energy for such a maximal extension was also measured to be $679.83 k_B T$ at 310 K, indicating that the maximally-stretched conformation is indeed a rare event on the free energy profile of the system, contrary to the initial structure as the energetically most-favorable conformation. It could also be inferred that performing such an extension within solution needs even a larger free energy according to the fact that enhancement in the entropy of the water molecules expelled from the hydrophobic core of the fibril is a key, stabilizing factor. The constant-force SMD trajectories further revealed the salt bridges that mostly contributed to the structural stability, as well as those that made the destabilizing core of the fibril. Applying replica-exchange umbrella sampling simulations, the unfolding probability of the fibril at the level of single β -strands was finally estimated, revealing the similar rareness for the spontaneous unfolding of the system as well.

Declaration of Competing Interest

The authors declare that they have no known competing financial interests or personal relationships that could have appeared to influence the work reported in this paper.

Data Availability Statement

The data supporting the findings of the present investigation are available on request from the corresponding author.

References

- [1] F. Chiti, C.M. Dobson, Protein misfolding, functional amyloid, and human disease, *Annu. Rev. Biochem.* 75 (2006) 333–366.
- [2] C. Haass, D.J. Selkoe, Soluble protein oligomers in neurodegeneration: lessons from the Alzheimer's amyloid β -peptide, *Nat. Rev. Mol. Cell. Biol.* 8 (2007) 101–112.
- [3] M. Goedert, Alzheimer's and Parkinson's diseases: the prion concept in relation to assembled A- β , tau, and α -synuclein, *Science* 349 (2015) 601.
- [4] I. Cherny, E. Gazit, Amyloids: not only pathological agents but also ordered nanomaterials, *Angew. Chem. Int. Ed.* 47 (2008) 4062–4069.
- [5] B. Choi, T. Kim, E.S. Ahn, S.W. Lee, K. Eom, Mechanical deformation mechanisms and properties of prion fibrils probed by atomistic simulations, *Nanoscale Res. Lett.* 12 (2017) 228.
- [6] T. Ackbarow, X. Chen, S. Keten, M.J. Buehler, Hierarchies, multiple energy barriers, and robustness govern the fracture mechanics of α -helical and β -sheet protein domains, *Proc. Natl. Acad. Sci. USA* 104 (2007) 16410–16415.
- [7] T.P.J. Knowles, M.J. Buehler, Nanomechanics of functional and pathological amyloid materials, *Nat. Nanotech.* 6 (2011) 469–479.
- [8] B. Choi, T. Kim, S.W. Lee, K. Eom, Nanomechanical characterization of amyloid fibrils using single-molecule experiments and computational simulations, *J. Nanomater.* 2016 (2016) 5873695.
- [9] J. Gosline, P. Guerette, C. Ortlepp, K. Savage, The mechanical design of spider silks: from fibroin sequence to mechanical function, *J. Exp. Biol.* 202 (1999) 3295–3303.
- [10] S. Keten, Z. Xu, B. Ihle, M.J. Buehler, Nanoconfinement controls stiffness, strength and mechanical toughness of β -sheet crystals in silk, *Nat. Mater.* 9 (2010) 359–367.
- [11] T.P. Knowles, A.W. Fitzpatrick, S. Meehan, H.R. Mott, M. Vendruscolo, C.M. Dobson, M.E. Welland, Role of intermolecular forces in defining material properties of protein nanofibrils, *Science* 318 (2007) 1900–1903.
- [12] J. Adamcik, J.-M. Jung, J. Flakowski, R.P. De Los, G. Dietler, R. Mezzenga, Understanding amyloid aggregation by statistical analysis of atomic force microscopy images, *Nat. Nanotech.* 5 (2010) 423–428.
- [13] J. Adamcik, A. Berquand, R. Mezzenga, Single-step direct measurement of amyloid fibrils stiffness by peak force quantitative nanomechanical atomic force microscopy, *Appl. Phys. Lett.* 98 (2011) 193701.
- [14] K.K.M. Sweers, K.O. van der Werf, M.L. Bennink, V. Subramaniam, Atomic force microscopy under controlled conditions reveals structure of C-terminal region of α -synuclein in amyloid fibrils, *ACS Nano* 6 (2012) 5952–5960.
- [15] G. Yoon, J. Kwak, J.I. Kim, S. Na, K. Eom, Mechanical characterization of amyloid fibrils using coarse-grained normal mode analysis, *Adv. Funct. Mater.* 21 (2011) 3454–3463.
- [16] G. Yoon, Y.K. Kim, K. Eom, S. Na, Relationship between disease-specific structures of amyloid fibrils and their mechanical properties, *Appl. Phys. Lett.* 102 (2013) 011914.
- [17] Z.P. Xu, R. Paparcone, M.J. Buehler, Alzheimer's A β (1–40) amyloid fibrils feature size-dependent mechanical properties, *Biophys. J.* 98 (2010) 2053–2062.
- [18] M. Solar, M.J. Buehler, Tensile deformation and failure of amyloid and amyloid-like protein fibrils, *Nanotechnology* 25 (2014) 105703.
- [19] M. Solar, M.J. Buehler, Comparative analysis of nanomechanics of protein filaments under lateral loading, *Nanoscale* 4 (2012) 1177–1183.
- [20] B. Choi, G. Yoon, S.W. Lee, K. Eom, Mechanical deformation mechanisms and properties of amyloid fibrils, *Phys. Chem. Chem. Phys.* 17 (2015) 1379–1389.

- [21] M.F.M. Engel, L. Khemttemourian, C.C. Kleijer, H.J.D. Meeldijk, J. Jacobs, A.J. Verkleij, B. de Kruijff, J.A. Killian, J.W.M. Höppener, Membrane damage by human islet amyloid polypeptide through fibril growth at the membrane, *Proc. Natl. Acad. Sci. USA* 105 (2008) 6033–6038.
- [22] S.E. Cross, Y.-S. Jin, J. Rao, J.K. Gimzewski, Nanomechanical analysis of cells from cancer patients, *Nat. Nanotech.* 2 (2007) 780–783.
- [23] A.W.P. Fitzpatrick, S.T. Park, A.H. Zewail, Exceptional rigidity and biomechanics of amyloid revealed by 4D electron microscopy, *Proc. Natl. Acad. Sci. USA* 110 (2013) 10976–10981.
- [24] H. Yu, A.N. Gupta, X. Liu, K. Neupane, A.M. Brigley, I. Sosova, M.T. Woodside, Energy landscape analysis of native folding of the prion protein yields the diffusion constant, transition path time, and rates, *Proc. Natl. Acad. Sci. USA* 109 (2012) 14452–14457.
- [25] A. Shekaari, M. Jafari, Non-equilibrium thermodynamic properties and internal dynamics of 32-residue beta amyloid fibrils, *Physica A* 557 (2020) 124873.
- [26] A. Shekaari, M. Jafari, arXiv:2103.16944v1.
- [27] R. Riek, D.S. Eisenberg, The activities of amyloids from a structural perspective, *Nature* 539 (2016) 227–235.
- [28] N. Agrawal, A.A. Skelton, 12-crown-4 ether disrupts the patient brain-derived amyloid- β fibril trimer: insight from all-atom molecular dynamics simulations, *ACS Chem. Neurosci.* 7 (2016) 1433–1441.
- [29] M. Gao, M. Wilmanns, K. Schulten, Steered molecular dynamics studies of titin i1 domain unfolding, *Biophys. J.* 83 (2002) 3435–3445.
- [30] <https://www.rcsb.org/>.
- [31] Y. Xiao, B. Ma, D. McElheny, S. Parthasarathy, F. Long, M. Hoshi, R. Nussinov, Y. Ishii, A beta (1-42) fibril structure illuminates self-recognition and replication of amyloid in Alzheimer’s disease, *Nat. Struct. Mol. Biol.* 22 (2015) 499–505.
- [32] J.C. Phillips, R. Braun, W. Wang, J. Gumbart, E. Tajkhorshid, E. Villa, C. Chipot, R.D. Skeel, L. Kale, K. Schulten, Scalable molecular dynamics with NAMD, *J. Comput. Chem.* 26 (2005) 1781–1802.
- [33] A.D. MacKerell Jr., D. Bashford, M. Bellott, R.L. Dunbrack Jr., J.D. Evanseck, M.J. Field, S. Fischer, J. Gao, H. Guo, S. Ha, D. Joseph-McCarthy, L. Kuchnir, K. Kuczera, F.T.K. Lau, C. Mattos, S. Michnick, T. Ngo, D.T. Nguyen, B. Prodhom, W.E. Reiher, B. Roux, M. Schlenkrich, J.C. Smith, R. Stote, J. Straub, M. Watanabe, J. Wiorkiewicz-Kuczera, D. Yin, M. Karplus, All-atom empirical potential for molecular modeling and dynamics studies of proteins, *J. Phys. Chem. B* 102 (1998) 3586–3616.
- [34] <https://www.debian.org>.
- [35] L. Torvalds, The Linux edge, *Commun. ACM* 42 (1999) 38–39.
- [36] <https://www.mpich.org>.
- [37] W. Gropp, E. Lusk, A. Skjellum, Using MPI: Portable Parallel Programming with the Message-Passing Interface, MIT Press, 1999.
- [38] W. Humphrey, A. Dalke, K. Schulten, VMD: visual molecular dynamics, *J. Mol. Graph.* 14 (1996) 33–38.
- [39] <http://jedi.ks.uiuc.edu/~johns/raytracer/>.
- [40] B. Lee, F.M. Richards, The interpretation of protein structures: estimation of static accessibility, *J. Mol. Biol.* 55 (1971) 379–400.
- [41] A. Shrake, J.A. Rupley, Environment and exposure to solvent of protein atoms. Lysozyme and insulin, *J. Mol. Biol.* 79 (1973) 351–371.
- [42] C. Jarzynski, Nonequilibrium equality for free energy differences, *Phys. Rev. Lett.* 78 (1997) 2690.
- [43] Y. Sugita, A. Kitao, Y. Okamoto, Multidimensional replica-exchange method for free-energy calculations, *J. Chem. Phys.* 113 (2000) 6042.
- [44] S. Kumar, D. Bouzida, R.H. Swendsen, P.A. Kollman, J.M. Rosenberg, The weighted histogram analysis method for free-energy calculations on biomolecules. I. The method, *J. Comput. Chem.* 13 (1992) 1011–1021.
- [45] <http://membrane.urmc.rochester.edu/sites/default/files/wham/wham-release-2.0.10.2.tgz>.
- [46] A. Shekaari, M. Jafari, arXiv:2102.05162.
- [47] <http://www.gnuplot.info>.
- [48] <https://www.gimp.org/>.

- [49] D. Frishman, P. Argos, Knowledge-based secondary structure assignment, *Proteins* 23 (1995) 566–579.
- [50] N. Agrawal, A.A. Skelton, Structure and function of Alzheimer’s amyloid β proteins from monomer to fibrils: A mini review, *Protein J.* 38 (2019) 425–434.
- [51] S. Cocco, R. Monasson, J.F. Marko, Force and kinetic barriers to unzipping of the DNA double helix, *PNAS* 98 (2001) 8608–8613.
- [52] R.K. Pathria, P.D. Beale, *Statistical Mechanics*, Third ed., Butterworth-Heinemann, Oxford, 2011.